Metal-Organic Framework-Derived Hybrid Co_3O_4-Carbon Porous Nanowire Arrays as Reversible Oxygen Evolution Electrodes

Tian Yi Ma,[†] Sheng Dai,[†] Mietek Jaroniec[‡] and Shi Zhang Qiao*,[†]

[†] School of Chemical Engineering, The University of Adelaide, Adelaide, SA 5005, Australia

[‡] Department of Chemistry and Biochemistry, Kent State University, Kent, Ohio 44240, USA

ABSTRACT: Hybrid porous nanowire arrays composed of strongly interacting Co_3O_4 and carbon were prepared by a facile carbonization of the metal-organic framework grown on Cu foil. The resulting material, possessing a high surface area of 251 m^2 g^{-1} and a large carbon content of 52.1 wt.%, can be directly used as the working electrode for oxygen evolution reaction without employing extra substrates or binders. This novel oxygen evolution electrode can smoothly operate in alkaline solutions (*e.g.* 0.1 M and 1.0 M KOH), affording a low onset potential of 1.47 V (*vs.* reversible hydrogen electrode) and a stable current density of 10.0 mA cm^{-2} at 1.52 V in 0.1 M KOH solution for at least 30 hours, associated with a high Faradaic efficiency of 99.3%. The achieved ultrahigh oxygen evolution activity and strong durability, superior performance as compared to the state-of-the-art noble-/transition-metal and non-metal catalysts, are originated from the unique nanowire array electrode configuration and *in situ* carbon incorporation, which lead to the large active surface area, enhanced mass/charge transport capability, easy release of oxygen gas bubbles and strong structural stability. Furthermore, the hybrid Co_3O_4-carbon porous nanowire arrays can also efficiently catalyze oxygen reduction reaction, featuring a desirable four-electron pathway for reversible oxygen evolution and reduction, which is potentially useful for rechargeable metal-air batteries, regenerative fuel cells and other important clean energy devices.

1. INTRODUCTION

Growing energy demands have stimulated a considerable interest in alternative energy conversion and storage systems such as metal-air batteries, water splitting devices and fuel cells, which are all closely associated with a core process, oxygen evolution reaction (OER) that is initiated at the boundary of multiple phases (solid, liquid, gas).[1] To rationally design the reaction interface for OER, an optimal electrode structure involving high-performance catalysts is essential in reducing the overpotential, promoting the reaction kinetics and enhancing the specific activity for OER, thus improving the energy efficiency.[2] However, most of the reported OER electrocatalysts, such as noble-metal (Ir, Ru),[3] transition-metal (Co, Mn, Ni, Fe, *etc.*)[4] and non-metal catalysts (graphitic carbon nitrides, N-doped graphitic carbons, *etc.*),[5] are generally prepared in the form of thin films or particle agglomerates coated onto glassy carbons, nickel foams or other conductive substrates. In most cases, these fabrication techniques require time-consuming film casting or coating procedures with assistance of polymeric binders, which result in uncontrolled micro-structure of the obtained electrodes featuring limited catalytically active surface areas that are unfavorable for electron conductivity and multiphase reactant/product transport during OER (*e.g.* OH^- in liquid phase, O_2 in gas phase). Also, the easy peeling of the coated catalysts from the electrodes during evolution of a large amount of O_2 greatly impairs their electrocatalytic activity and shelf life.[6] Thus, the development of alternative electrode configurations for efficiently catalyzed

OER with high activity and strong long-term stability is urgently needed.

Recently, the well-aligned nanowire arrays with catalytically active components directly grown on the current collectors have been considered as a new generation of highly effective electrodes due to their intrinsic advantages.[7] The open space within nanowire arrays facilitates the electrolyte penetration and diffusion of ionic species, allowing high utilization efficiency of active species. The direct contact of nanowire arrays with the underneath conductive current collectors and their strong binding assure good electrical conductivity between them, as well as high structural stability of the obtained electrodes.[6b,c,7,8] Thus, these electrodes show great potential for direct use in electrochemical cells, and they are particularly beneficial for OER that involves continuous evolution of O_2 gas.[1,3-5]

Nevertheless, the use of nanowire arrays for electrocatalytic OER is still in its infancy. Only a few illustrations including $Zn_xCo_{3-x}O_4$ and $Ni_xCo_{3-x}O_4$ nanowire arrays grown on Ti foils,[9] Co_3O_4 nanowire arrays grown on the stainless steel meshes,[10] and Ni-substituted Co_3O_4 nanowire arrays grown on Ni foams[11] were reported, all focusing on Co_3O_4-based spinel materials due to their good catalytic activity and corrosion stability toward electrochemical OER in alkaline media.[12] Their fabrication unexceptionally involved nucleation and growth of inorganic precursors on certain substrates, and was limited to pure metal oxides.[9-11] However, the semiconducting metal oxide nanowires having the length of several micrometers do not assure a continuous pathway for electron transport along them.[7] Also, the mass transport and accessible catalytically active sites associated with individual nanowires are

limited due to the low porosity and relatively small surface area of the nanowires.[9-11] Therefore, further improvement of this type of electrodes is highly expected, especially through increasing the electrical conductivity of single nanowires by elemental doping or other methods, and through introducing accessible pores into the nanowires.

To achieve these goals, we design the first hybrid Co_3O_4-carbon porous nanowire arrays (denoted as Co_3O_4C-NA), which are prepared by carbonization of the metal-organic framework (MOF) directly grown on Cu foil in N_2 atmosphere. The periodic arrangement of metal nodes and organic motifs in MOF scaffolds leads to a homogeneous distribution of metal oxide nanoparticles and *in situ* formed carbon species. Our purpose is to accomplish better catalytic performance of the hybrid nanowire array electrode by combining distinctive properties of metal oxide and carbon components, and taking advantage of their uniform distribution and synergy.[13] Herein, the use of Co-based MOF as the precursor represents a facile way of obtaining Co_3O_4C-NA with the high surface area and large carbon content. Remarkably, Co_3O_4C-NA not only exhibits better oxygen evolution activity and stronger durability than most of the highly active noble-/transition-metal and non-metal catalysts reported to date, but also efficiently catalyzes the reverse oxygen reduction reaction (ORR). Its outstanding activity can be attributed to the large active surface area, favorable charge and mass transport in the stable nanowire array electrode structure.

2. RESULTS AND DISCUSSION

2.1. CATALYST SYNTHESIS AND CHARACTERIZATION
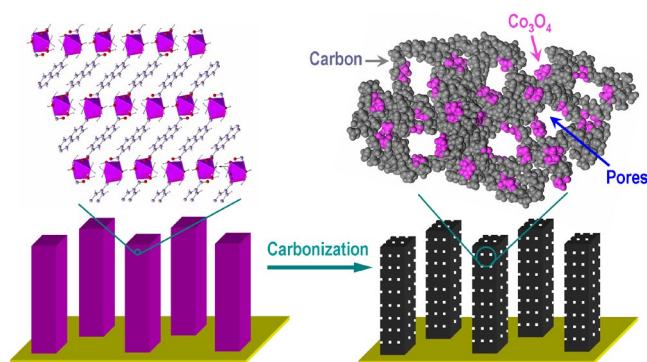
Scheme 1. Fabrication of hybrid Co_3O_4-carbon porous nanowire arrays.

The hybrid Co_3O_4-carbon porous nanowire arrays were synthesized from a Co-naphthalenedicarboxylate MOF with layered crystalline structure used as the precursor (Scheme 1), which was directly grown on Cu foil through a low-temperature (80 ºC) hydrothermal process. Next, the inorganic and organic components in the MOF were converted, respectively, into Co_3O_4 and carbon via carbonization in N_2 atmosphere, which resulted in the formation of hybrid nanowires with simultaneously generated pores inside.
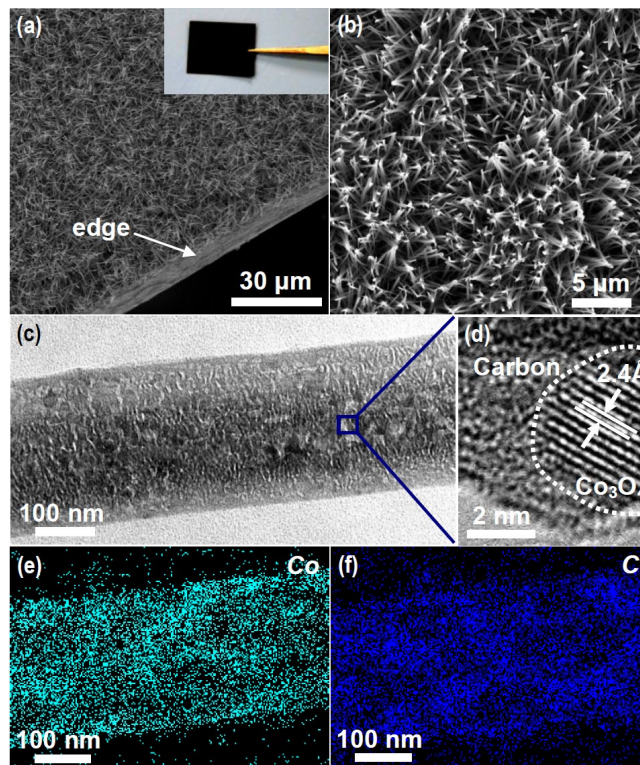

Figure 1. (a, b) SEM, (inset in panel a) optical image, (c) TEM, (d) HRTEM, and (e, f) EDS elemental mapping images of Co_3O_4C-NA.

Nanowire arrays of Co_3O_4C-NA (scanning electron microscopy (SEM), Figures 1a, b), preserving the morphology of the Co-based MOF (Figure S1, Supporting Information), grow on the surface of Cu foil, the color of which turns to black (Figure 1a inset). A single nanowire with smooth surface and the diameter of ~250 nm is observed in the transmission electron microscopy (TEM) image (Figure 1c). Nanowires obtained with high yield and without presence of morphologically different particles and their smooth surface indicate that all Co_3O_4 and carbon species are well integrated inside them with negligible amount of isolated Co_3O_4 nanocrystals. Numerous slit-like pores visible throughout the nanowire are preferably generated via deterioration and carbonization of the alternating organic naphthalene layers,[13] which agrees well with the layered crystalline structure of the MOF (Figure S2). The high-resolution transmission electron microscopy (HRTEM) image (Figure 1d) presents apparently different domains of amorphous carbon and crystalline Co_3O_4, with clearly identified lattice fringe space of 2.4 Å corresponding to the (311) plane of cubic Co_3O_4 spinel-phase. Notably, Co species catalyze the formation of partially graphitized carbon on the surface of Co_3O_4. The HRTEM observation is also consistent with the uniform dispersion of Co and C elements in Co_3O_4C-NA (energy dispersive X-ray spectroscopy (EDS) elemental mapping image, Figures 1e, f), together verifying the homogeneous distribution of closely interconnected Co_3O_4 and carbon species.
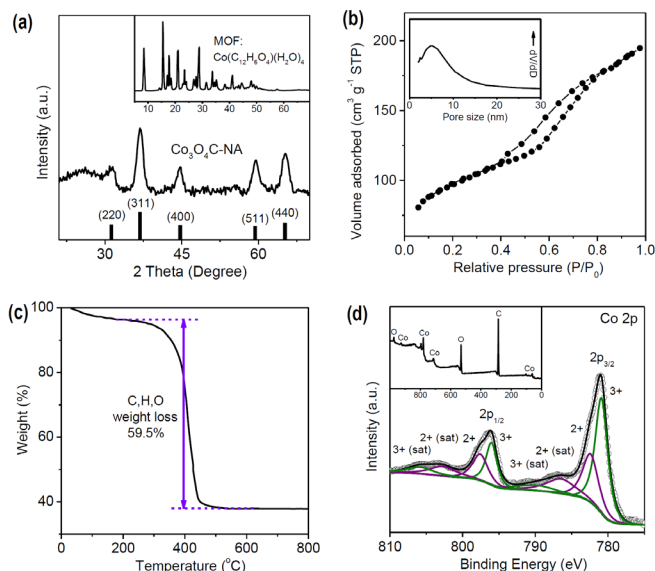
Figure 2. XRD patterns of (a) Co₃O₄C-NA and (inset in panel a) the MOF used as the precursor. (b) N₂ adsorption isotherm and (inset in panel b) the corresponding pore size distribution of Co₃O₄C-NA. (c) TG curve of Co₃O₄C-NA. (d) High-resolution XPS spectrum of Co 2p core level and (inset in panel d) XPS survey spectrum of Co₃O₄C-NA.

The multiple peaks on the X-ray diffraction (XRD) pattern of the Co-based MOF used (inset in **Figure 2a**) well match those of the typical crystalline structure of $Co(C_{12}H_6O_4)(H_2O)_4$,[14] without detectable peaks from cobalt oxides. After carbonization, Co₃O₄C-NA exhibits the cubic spinel-phase structure (JCPDS No. 43-1003) with a broad shoulder peak in the range of 20 to 30° (2θ), which is originated from the amorphous carbon species homogeneously distributed in nanowires that are in situ formed during carbonization process (**Figure 2a**), as evidenced by HRTEM and EDS. The N₂ adsorption isotherm recorded on Co₃O₄C-NA resembles type IV with a H3 type hysteresis loop (**Figure 2b**), commonly observed for materials with slit-like mesopores,[15] which agrees well with TEM observation and the layered crystalline structure of the MOF used. Correspondingly, one peak centered at ~5 nm is found in the pore size distribution curve. Also, Co₃O₄C-NA displays a large surface area of 251 m² g⁻¹, which is much higher than that of the Co-based MOF used (**Figure S3**) and other reported nanowire arrays prepared by inorganic precursors (up to ~100 m² g⁻¹),[7,9-11] indicating the superiority of our proposed method for creating highly porous hybrid nanowires from MOF via the carbonization process.

The hybrid nature of nanowire arrays was further confirmed by thermogravimetric analysis (TG, **Figure 2c**). Besides the 3% weight loss below 200 °C due to the adsorbed water and gases, the weight loss of 59.5% in Co₃O₄C-NA between 200 to 500 °C is ascribed to the combustion of carbon species with some surface-bonded oxygen-containing functional groups, which is consistent with the elemental analysis showing the carbon content of 52.1 wt.%. X-ray photoelectron spectra (XPS) indicate that Co₃O₄C-NA contains Co, C and O elements without other impurities, and the best deconvolution of Co 2p profile was achieved under assumption of eight species including two pairs of spin-orbit doublets indicating the coexistence of Co²⁺ and Co³⁺ and their four shake-up satellites (denoted as 'sat', **Figure 2d**).[16] As compared to the XPS peak

centered at 780.1 eV assigned to Co 2p₃/₂ of pure Co₃O₄ (**Figure S4**), the shift of the corresponding peak of Co₃O₄C-NA to 781.2 eV implies the close assembly and strong interaction between Co₃O₄ and carbon, resulting in the impaired electron density of Co atoms in Co₃O₄C-NA.[17] Therefore, TEM, EDS and XPS demonstrate homogenously dispersed and well interacting nanocrystalline Co₃O₄ and conductive carbon species in Co₃O₄C-NA, which is desired for high-performance electrocatalysts.

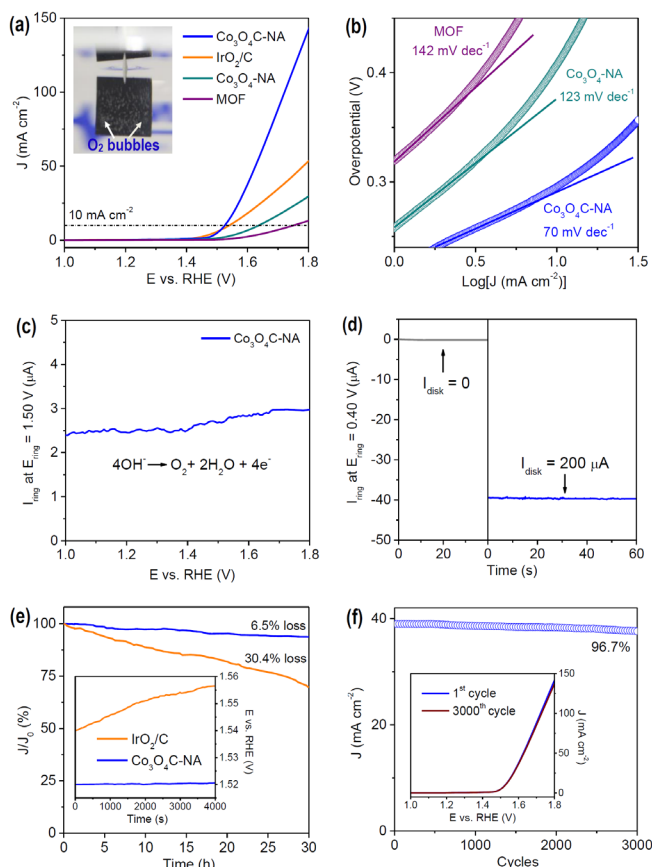## 2.2. OXYGEN EVOLUTION ACTIVITY

Figure 3. (a) Polarization curves and (b) Tafel plots of Co₃O₄C-NA, IrO₂/C, Co₃O₄-NA, and the MOF in an O₂-saturated 0.1 M KOH solution (scan rate: 0.5 mV s⁻¹). (Inset in panel a) An optical image of Co₃O₄C-NA directly used as the OER electrode operating at 1.70 V with generated bubbles on the surface indicating the formation of O₂ gas. (c) The ring current of Co₃O₄C-NA on a RRDE (1500 rpm) in O₂-saturated 0.1 M KOH solution (ring potential: 1.50 V). (d) The ring current of Co₃O₄C-NA on a RRDE (1500 rpm) in N₂-saturated 0.1 M KOH solution (ring potential: 0.40 V). (e) Chronoamperometric response at a constant potential of 1.52 V ($E_{j=10}$), and (inset in panel e) chronopotentiometric response at a constant current density of 10.0 mA cm⁻² of Co₃O₄C-NA as compared to that of IrO₂/C. (f) A plot of the current density at 1.60 V recorded from the polarization curve of Co₃O₄C-NA *vs.* the cycle number, and (inset in panel f) polarization curves of Co₃O₄C-NA before and after 3000 potential cycles (scan rate: 100 mV s⁻¹).

Sizable and shapeable electrodes can be prepared by simply tailoring the Cu foil, and the obtained Co₃O₄C-NA grown on Cu foil can be directly used as the working electrode for OER (**Figures 3a** inset, **S5**, **Video S1**) without employing extra substrates (*e.g.* glassy carbon electrode) or binders (*e.g.*

nafion). A slow scan rate (0.5 mV s^{-1}) was applied during the OER test to minimize the capacitive current. Since Co$_3$O$_4$ nanocrystals may partially dissolve in acidic solutions such as H$_2$SO$_4$, alkaline eletrolytes (0.1 M and 1.0 M KOH) are prefered for the catalyst studied and examined in this work. The Cu foil exhibits negligible catalytic activity as shown in the polarization curve conducted in 0.1 M KOH solution (**Figure S6**), and the Co-based MOF also displays low OER response with a high onset potential at ~1.55 V *vs.* reversible hydrogen electrode (RHE, **Figure 3a**); while the anodic current recorded on Co$_3$O$_4$C-NA renders a sharp onset potential at ~1.47 V with greatly enhanced OER current, indicating that the compositional transformation of MOF to hybrid Co$_3$O$_4$-carbon can significantly improve the catalytic activity. Noticeably, the OER current of Co$_3$O$_4$C-NA largely exceeds that of IrO$_2$/C (coated on Cu foil with the same loading amount and carbon content to that of Co$_3$O$_4$C-NA, see synthesis details in Supporting Information), despite of the slightly lower onset potential of IrO$_2$/C (~1.45 V), featuring much better catalytic performance of Co$_3$O$_4$C-NA.

We further compared the operating potentials required for different catalysts to deliver a 10.0 mA cm^{-2} current density ($E_{j=10}$), which is a metric related to solar fuel synthesis.[18] Co$_3$O$_4$C-NA affords a current density of 10.0 mA cm^{-2} at 1.52 V, lower than that of IrO$_2$/C at 1.54 V and many other reported noble-metal catalysts.[3b,5c,19] Moreover, this excellent OER activity of Co$_3$O$_4$C-NA is not only better than that of most of the state-of-the-art Co-based transition-metal electrocatalysts,[4d,e,17a,18,20] and non-metal catalysts,[5] but also superior to that of all the nanowire array electrodes reported to date, *i.e.* Zn$_x$Co$_{3-x}$O$_4$ nanowire arrays grown on Ti foils (1.55 V, pH 14),[9a] Ni$_x$Co$_{3-x}$O$_4$ nanowire arrays grown on Ti foils (~1.60 V, pH 14),[9b] and Ni-substituted Co$_3$O$_4$ nanowire arrays grown on Ni foams (~1.60 V, pH 14).[11] A detailed comparison of different highly active OER catalyts with various electrode configurations is shown in **Table S1**, further confirming the outstanding catalytic behavior of Co$_3$O$_4$C-NA. Also, the catalytic kinetics for oxygen evolution was examined by Tafel plots (**Figure 3b**). The Tafel slope value of Co$_3$O$_4$C-NA (70 mV decade^{-1}) is lower than that of the Co-based MOF (142 mV decade^{-1}) and IrO$_2$/C (97 mV decade^{-1}, **Figure S7**), and comparable to that of the previously reported highly active OER catalyts (**Table S1**), suggesting its favorable reaction kinetics.

To investigate the reaction mechanism, the rotating ring-disk electrode (RRDE) technique was employed with a Pt ring electrode potential of 1.50 V to oxidize the peroxide intermediates formed at the Co$_3$O$_4$C-NA surface during OER. Co$_3$O$_4$C-NA was scraped off from Cu foil and coated on a RRDE (see experimental details in Supporting Information). As shown in **Figure 3c**, a very low ring current (μA scale) was detected, which is three orders of magnitude lower than that of the disk current (mA scale), suggesting negligible hydrogen peroxide formation and therefore a desirable four-electron pathway for water oxidation, *i.e.* 4OH$^-$ → O$_2$ + 2H$_2$O + 4e$^-$. Furthermore, to confirm that the observed current originates from water oxidation rather than other side reactions and to calculate the Faradaic efficiency, a RRDE with the ring potential of 0.40 V was applied to reduce the generated O$_2$, rendering a continuous OER (disk electrode) → ORR (ring electrode) process (**Figure S8**). With the disk current held constantly at 200 μA, O$_2$ molecules generated from the Co$_3$O$_4$C-NA catalyst surface on the disk electrode sweep

across the surrounding Pt ring electrode that is held at an ORR potential, and are rapidly reduced. Consequently, a ring current of ~39.7 μA (collection efficiency = 0.2) was detected (**Figure 3d**), which verifies the observed oxidation current catalyzed by Co$_3$O$_4$C-NA can be fully attributed to OER with a high Faradaic efficiency of 99.3% (see detailed calculation in Supporting Information).

Strong durability toward OER is of great significance for energy conversion and storage systems. The chronoamperometric response demonstrates the high stability of Co$_3$O$_4$C-NA, showing slight anodic current attenuation of 6.5% within 30 hours, whereas IrO$_2$/C displays a 4.7 times larger current attenuation of 30.4% (**Figures 3e, S9**), indicating the apparent advantage of active materials directly grown on conductive substrates as compared to the post-coated catalysts on electrodes, because the latter suffer from peeling off during the evolution of a large amount of O$_2$ gas.[3-5] The XRD pattern of the catalyst after 30-hour reaction shows no phase change as compared to the fresh Co$_3$O$_4$C-NA (**Figure S10**), which corroborates that the hybrid Co$_3$O$_4$-carbon nanowire arrays act as highly OER-active and stable catalysts. In the chronopotentiometric response, Co$_3$O$_4$C-NA affords a nearly constant operating potential of 1.52 V to deliver a 10.0 mA cm^{-2} current density (**Figure 3e** inset), whereas the potential of IrO$_2$/C increases for > 15 mV within 4000 s, again revealing the stronger durability of Co$_3$O$_4$C-NA. Further, only 3.3% anodic current loss was observed for Co$_3$O$_4$C-NA after 3000 continuous potential cyclings at an accelerated scanning rate of 100 mV s^{-1} (**Figure 3f**), confirming the catalyst is also highly stable to withstand accelerated degradation.

The effective operation of electrocatalysts in concentrated electrolytes is a critical figure of merit for practical applications.[18] In 1.0 M KOH, the high activity of Co$_3$O$_4$C-NA is well preserved showing larger current density, and much lower Tafel slope of 61 mV decade^{-1} than that of IrO$_2$/C (87 mV decade^{-1}, **Figures S11a, b**), indicating the superior reaction kinetics of Co$_3$O$_4$C-NA. Both the chronoamperometric and chronopotentiometric responses show much smaller OER activity attenuation of Co$_3$O$_4$C-NA in comparison to that of IrO$_2$/C (**Figures S11c, d**), demonstrating the strong durability of Co$_3$O$_4$C-NA in concentrated alkaline solutions.
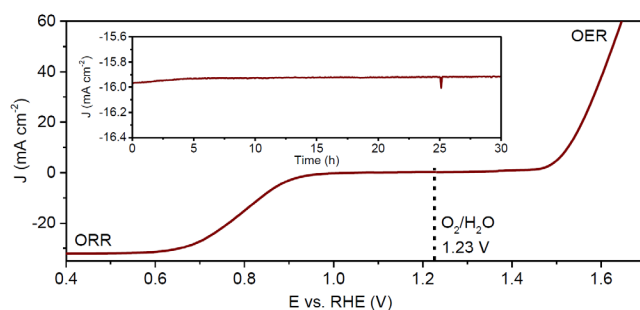

Figure 4. Polarization curve measured in O$_2$-saturated 0.1 M KOH solution (scan rate: 0.5 mV s^{-1}) for Co$_3$O$_4$C-NA grown on Cu foil (directly used as the working electrode) in the whole region of OER and ORR. (Inset in the panel) chronoamperometric response of Co$_3$O$_4$C-NA at a constant potential of 0.78 V ($E_{1/2}$), with methanol addition after 25 h.

The reaction reversibility initiated on an oxygen evolution electrode, which can also efficiently catalyze the reverse ORR

process, is of significant importance, especially for rechargeable metal-air batteries and regenerated fuel cells involving these two reactions. Thus, polarization curves were recorded in the whole region of OER and ORR. In ORR region, Co_3O_4C-NA exhibits a half-wave potential ($E_{1/2}$) of 0.78 V (**Figure 4**) and Tafel slope of 89 mV decade^{-1} (**Figure S12a**). The overall oxygen electrode activity can be evaluated by the difference of OER and ORR metrics ($\Delta E = E_{j=10} - E_{1/2}$). The smaller ΔE is, the closer the catalyst is to an ideal reversible oxygen electrode.[21] Co_3O_4C-NA exhibits a ΔE value of 0.74 V, lower than that of the recently reported highly active reversible oxygen electrodes, e.g. CoO/N-doped graphene (ΔE = 0.76 V),[20a] Co_3O_4/N-doped carbon (ΔE = 0.86 V)[21a] and H-Pt/CaMnO$_3$ (ΔE = 1.01 V),[21b] corroborating the excellent reversible oxygen electrode nature of Co_3O_4C-NA. Further, combining RRDE measurements that suggest an electron transfer number of 3.85−3.96 (from 0.40 V to 0.90 V) for the ORR process (**Figure S12b**), Co_3O_4C-NA favors a desirable four-electron pathway for reversible OER and ORR. Moreover, Co_3O_4C-NA shows a strong durability for ORR as revealed by the chronoamperometric response (**Figure 4** inset), delivering a nearly constant current density within 30 hours. Notably, the current density of Co_3O_4C-NA shows no obvious change even after the addition of methanol, indicating its high selectivity to ORR with strong methanol tolerance ability, which can avoid the poisoning cross-over effect, displaying an important quality for cathode materials in low-temperature fuel cells.

2.3. DISCCUSION

The unique hybrid nanowire composition and novel electrode configuration endow Co_3O_4C-NA with much better catalytic performance than conventional electrode materials. First, the in situ incorporation of carbon into Co_3O_4C-NA assured by the use of MOF as the precursor, leads to the structure with strongly interacting Co_3O_4 and carbon species (as evidenced by TEM, EDS and XPS), and highly improved conductivity and charge transfer capability, which favor the high OER activity and stability. For the purpose of comparison, a carbon-free counterpart was prepared by calcination of Co_3O_4C-NA in air to eliminate carbon species (denoted as Co_3O_4-NA, see synthesis details in Supporting Information), which also exhibits porous nanowire array structure and cubic spinel phase (**Figures S3, S13**), but affords higher onset potential of 1.50 V, larger operating potential of 1.64 V to deliver a 10.0 mA cm^{-2} current density (**Figure 3a**), and higher Tafel slope of 123 mV decade^{-1} (**Figure 3b**) than those of Co_3O_4C-NA, suggesting its much lower OER activity with inferior reaction kinetics. Also, the semicircle diameter in the electrochemical impedance spectrum (EIS) of Co_3O_4-NA is much larger than that of Co_3O_4C-NA due to smaller contact and charge transfer impedance in Co_3O_4C-NA (**Figure 5a**). Notably, Co_3O_4C-NA also largely exceeds the physically mixed Co_3O_4-NA and carbon powder in OER performance (**Figure 5b**, see synthesis details in Supporting Information), which implies that the outstanding activity of Co_3O_4C-NA with low resistance originates not simply from the increased electrical conductivity, but also from a complex synergistic effect between strongly interacting Co_3O_4 and carbon species.[17] For instance, the in situ incorporated carbon causes the impaired electron density of Co atoms (as evidenced by XPS), which can make the catalytically active species (i.e. Co) more electrophilic, thus facilitating the adsorption and reaction of OH$^-$ groups with Co_3O_4C-NA, resulting in enhanced OER activity in alkaline solutions.[22]

Second, the mesoporous nanowire arrays afford a large active surface area, which was evaluated by the electrochemical double layer capacitance (C_{dl}) and surface roughness factor (R_f). By calculating the slope from the linear relationship of the current density against the scan rate (see calculation details in Supporting Information), C_{dl} of Co_3O_4C-NA is confirmed to be 209.7 mF cm^{-2} with a R_f of 3495 (**Figure 5c**), which is much higher than that of IrO$_2$/C (C_{dl} = 22.3 mF cm^{-2}, R_f = 371, **Figure S14**). Since C_{dl} and R_f are proportional to the active surface area of electrocatalysts,[7-11] the results demostrate mesoporous nanowire arrays directly grown on Cu foil are more effective in enlarging the catalytically active surface area as compared to conventioanl planar catalyst films coated on electrodes; thus, better exposure and enhanced utilization of electroactive sites (e.g. Co species) on the large active surface of Co_3O_4C-NA greatly contribute to its ultrahigh OER activity.

Third, the reaction kinetics for OER is significantly promoted by the advanced electrode configuration. The nanowire arrays provide smooth pathway for fast penetration of electrolyte, while the mesopores facilitate the access of reactants (e.g. OH$^-$) in the electrolyte to the active sites within nanowires, as well as the fast emission of reaction products (e.g. O$_2$). Accordingly, Co_3O_4C-NA displays much smaller Tafel slope than that of IrO$_2$/C, physically mixed Co_3O_4-NA and carbon powder, and other catalysts in the control group (**Figures 3b, 5b** inset, **S7, S11b**), indicating its more favorable reaction kinetics. Also, its current density in OER potential region is insusceptible to the scan rate, showing a variation of 3.5% (vs. 14.3 % of IrO$_2$/C) with increasing the scan rate from 0.5 mV s^{-1} to 50 mV s^{-1} (**Figure S15**), due to the improved mass transport in the mesoporous nanowire arrays.[5,7] Additionally, the micro-structure of nanowire arrays is believed to promote the release of evolved O$_2$ gas bubbles (**Video S1**), by effectively bursting larger O$_2$ bubbles that commonly stick to the planar catalyst film surface, and wicking the evolved bubbles to maintain the solid-liquid interface.[23]
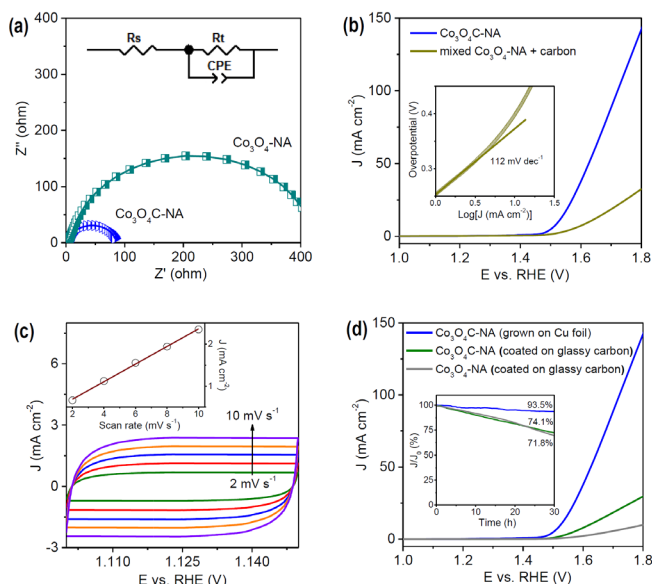

Figure 5. (a) EIS of Co_3O_4C-NA and Co_3O_4-NA recorded at 1.60 V, and (inset in panel a) the corresponding equivalent circuit diagram consisting of an electrolyte resistance (Rs), a charge-transfer resistance (Rt) and a constant-phase element (CPE). (b) Polariza-

tion curves of Co₃O₄C-NA directly grown on Cu foil and physically mixed Co₃O₄-NA and carbon powder coated on Cu foil, and (inset in panel b) Tafel plot of the physically mixed Co₃O₄-NA and carbon powder. (c) Cyclic voltammograms (CVs) of Co₃O₄C-NA measured at different scan rates from 2 to 10 mV s⁻¹, and (inset in panel c) a plot of the current density at 1.14 V *vs.* the scan rate. (d) Polarization curves of Co₃O₄C-NA directly grown on Cu foil, Co₃O₄C-NA and Co₃O₄-NA scraped off from Cu foil and coated on glassy carbon electrodes, and (inset in panel d) the corresponding chronoamperometric response at a constant potential of 1.52 V.

Last but not least, the direct growth of active materials on the conductive Cu foil can greatly enhance the electron transport and adhesion between nanowire arrays and substrates, promote the structural stability for long-term usage, and avoid utilization of polymeric binders and extra conductive additives, consequently reducing the dead volume and undesirable interface in the electrode,[9-11,12b] which is corroborated by the much higher OER activity and stronger durability of Co₃O₄C-NA than those of IrO₂/C coated on Cu foil (**Figure 3e**), and those of Co₃O₄-NA and Co₃O₄C-NA scraped off from Cu foil and coated on traditional glassy carbon electrodes (**Figure 5d**). Also, even operating at a high potential of 1.80 V (delivering a very large current density of ~140 mA cm⁻²), Co₃O₄C-NA shows no visible peeling from Cu foil (**Video S1**), suggesting the strong stability of this type of oxygen evolution electrodes.

3. CONCLUSIONS

In summary, hybrid Co₃O₄-carbon porous nanowire arrays directly grown on Cu foil exhibit higher OER activity, more favorable kinetics and stronger durability than those of IrO₂/C. The OER performance is the best among all the reported nanowire array electrodes, and better than most of the highly active noble-/transition-metal and non-metal OER catalysts, which can be attributed to the porous nanowire array electrode configuration and *in situ* carbon incorporation, leading to enlarged active surface area, strong structural stability, and improved mass/charge transport. Considering their capability for catalyzing ORR through an efficient four-electron pathway, these brand new reversible oxygen electrodes are promising to be directly used in metal-air batteries, fuel cells, water splitting devices and other key renewable energy systems.

ASSOCIATED CONTENT

Supporting Information. Experimental details; SEM images, crystalline structure with the CIF file and N₂ adsorption of the Co-based MOF; XPS, XRD, SEM images and N2 adsorption of Co₃O₄-NA; optical photos of three-electrode OER testing cells; OER activity and stability tests of Co₃O₄C-NA in 1.0 M KOH; polarization curves, Tafel plots and stability tests of control groups; Tafel plot, electron transfer number and HO₂⁻ production curves for ORR of Co₃O₄C-NA; a detailed comparisom of various OER catalysts; and a video of Co₃O₄C-NA working at different operating potentials. This material is available free of charge via the Internet at http://pubs.acs.org.

AUTHOR INFORMATION

Corresponding Author

* E-mail: s.qiao@adelaide.edu.au

Author Contributions

All authors have given approval to the final version of the manuscript.

REFERENCES

1. a) Kim, T. W.; Choi, K. S. *Science* **2014**, *343*, 990−994; b) Zhang, M.; de Respinis, M.; Frei, H. *Nat. Chem.* **2014**, *6*, 362−367; c) Yuan, C. Z.; Wu, H. B.; Xie, Y.; Lou, X. W. *Angew. Chem.* **2014***, 126,* 1512−1530; *Angew. Chem. Int. Ed.* **2014**, *53*, 1488−1504.

2. a) Katsounaros, I.; Cherevko, S.; Zeradjanin, A. R.; Mayrhofer, K. J. J. *Angew. Chem.* **2014***, 126,* 104−124; *Angew. Chem. Int. Ed.* **2014**, *53*, 102−121; b) Oh, S. H.; Black, R.; Pomerantseva, E.; Lee, J. H.; Nazar, L. F. *Nat. Chem.* **2012**, *4*, 1004−1010.

3. a) Over, H. *Chem. Rev.* **2012**, *112*, 3356−3426; b) Lee, Y.; Suntivich, J.; May, K. J.; Perry, E. E.; Shao-Horn, Y. *J. Phys. Chem. Lett.* **2012**, *3*, 399−404.

4. a) Jin, K.; Park, J.; Lee, J.; Yang, K. D.; Pradhan, G. K.; Sim, U.; Jeong, D.; Jang, H. L.; Park, S.; Kim, D.; Sung, N. E.; Kim, S. H.; Han, S.; Nam, K. T. *J. Am. Chem. Soc.* **2014**, *136*, 7435−7443; b) Gong, M.; Li, Y. G.; Wang, H. L.; Liang, Y. Y.; Wu, J. Z.; Zhou, J. G.; Wang, J.; Regier, T.; Wei, F.; Dai, H. J. *J. Am. Chem. Soc.* **2013**, *135*, 8452−8455; c) Subbaraman, R.; Tripkovic, D.; Chang, K. C.; Strmcnik, D.; Paulikas, A. P.; Hirunsit, P.; Chan, M.; Greeley, J.; Stamenkovic, V.; Markovic, N. M. *Nat. Mater.* **2012**, *11*, 550−557; d) Gao, M. R.; Xu, Y. F.; Jiang, J.; Zheng, Y. R.; Yu, S. H. *J. Am. Chem. Soc.* **2012**, *134*, 2930−2933; e) Liang, Y. Y.; Li, Y. G.; Wang, H. L.; Zhou, J. G.; Wang, J.; Regier, T.; Dai, H. J. *Nat. Mater.* **2011**, *10*, 780−786.

5. a) Ma, T. Y.; Dai, S.; Jaroniec, M.; Qiao, S. Z. *Angew. Chem.* **2014**, *126*, 7409−7413; *Angew. Chem. Int. Ed.* **2014**, *53*, 7281– 7285; b) Tian, G. L.; Zhao, M. Q.; Yu, D.; Kong, X. Y.; Huang, J. Q.; Zhang, Q.; Wei, F. *Small* **2014**, *10*, 2251–2259; c) Zhao, Y.; Nakamura, R.; Kamiya, K.; Nakanishi, S.; Hashimoto, K. *Nat. Commun.* **2013**, *4*, 2390; d) Park, H. W.; Lee, D. U.; Liu, Y.; Wu, J.; Nazar, L. F.; Chen, Z. *J. Electrochem. Soc.* **2013**, *160*, A2244–A2250.

6. a) Wang, J.; Zhong, H. X.; Qin, Y. L.; Zhang, X. B. *Angew. Chem.* **2013**, *125*, 5356–5361; *Angew. Chem. Int. Ed.* **2013**, *52*, 5248–5253; b) Xin, S.; Guo, Y. G.; Wan, L. J. *Acc. Chem. Res.* **2012**, *45*, 1759–1769; c) Cheng, F. Y.; Chen, J. *Chem. Soc. Rev.* **2012**, *41*, 2172–2192; d) Kibsgaard, J.; Gorlin, Y.; Chen, Z.; Jaramillo, T. F. *J. Am. Chem. Soc.* **2012**, *134*, 7758–7765; e) Lang, X. Y.; Hirata, A.; Fujita, T.; Chen, M. W. *Nat. Nanotechnol.* **2011**, *6*, 232–236.

7. a) Wang, K.; Wu, H.; Meng, Y.; Wei, Z. *Small* **2014**, *10*, 14– 31; b) Shen, L.; Che, Q.; Li, H.; Zhang, X. *Adv. Funct. Mater.* **2014***, 24*, 2630–2637; c) Jiang, Y.; Zhang, X.; Ge, Q. Q.; Yu, B. B.; Zou, Y. G.; Jiang, W. J.; Song, W. G.; Wan, L. J.; Hu, J. S. *Nano Lett.* **2014**, *14*, 365–372; d) Tian, J. Q.; Liu, Q.; Asiri, A. M.; Sun, X. P. *J. Am. Chem. Soc.* **2014**, *136*, 7587−7590; e) Liao, J. Y.; Higgins, D.; Lui, G.; Chabot, V.; Xiao, X.; Chen, Z. *Nano Lett.* **2013**, *13*, 5467−5473; f) Yuan, C.; Yang, L.; Hou, L.; Shen, L.; Zhang, X.; Lou, X. W. *Energy Environ. Sci.* **2012**, *5*, 7883–7887.

8. a) Jiang, J.; Li, Y.; Liu, J.; Huang, X.; Yuan, C.; Lou, X. W. *Adv. Mater.* **2012**, *24*, 5166–5180; b) Gong, K.; Du, F.; Xia, Z.; Durstock, M.; Dai, L. M. *Science* **2009**, *323*, 760–764.

9. a) Liu, X. J.; Chang, Z.; Luo, L.; Xu, T. H.; Lei, X. D.; Liu, J. F.; Sun, X. M. *Chem. Mater.* **2014**, *26*, 1889–1895; b) Li, Y.; Hasin, P.; Wu, Y. *Adv. Mater.* **2010**, *22*, 1926–1929.

10. Lee, D. U.; Choi, J. Y.; Feng, K.; Park, H. W.; Chen, Z. *Adv. Energy Mater.* **2014**, *4*, 1301389.

11. Lu, B.; Cao, D.; Wang, P.; Wang, G.; Gao, Y. *Int. J. Hydrogen Energy* **2011**, *36*, 72–78.

12. a) Artero, V.; Chavarot-Kerlidou, M.; Fontecave, M. *Angew. Chem.* **2011**, *123*, 7376–7405; *Angew. Chem. Int. Ed.* **2011**, *50*, 7238–7266; b) Cui, B.; Lin, H.; Li, J. B.; Li, X.; Yang, J.; Tao, J. *Adv. Funct. Mater.* **2008**, *18*, 1440–1447.

13. a) Sun, J. K.; Xu, Q. *Energy Environ. Sci.* **2014**, *7*, 2071–2100; b) Proietti, E.; Jaouen, F.; Lefèvre, M.; Larouche, N.; Tian, J.; Herranz, J.; Dodelet, J. P. *Nat. Commun.* **2011**, *2*, 416; c) Furukawa, H.; Cordova, K. E.; O'Keeffe, M.; Yaghi, O. M. *Science* **2013**, *341*, 1230444.

14. Kaduk, J. A.; Hanko, J. A. *J. Appl. Cryst.* **2001**, *34*, 710–714.

15. Gu, D.; Schüth, F. *Chem. Soc. Rev.* **2014**, *43*, 313–344.

16. Banerjee, D.; Jagadeesh, R. V.; Junge, K.; Pohl, M. M.; Radnik, J.; Brückner, A.; Beller, M. *Angew. Chem.* **2014**, *126*, 4448–4452; *Angew. Chem. Int. Ed.* **2014**, *53*, 4359–4363.

17. a) Wu, J.; Xue, Y.; Yan, X.; Yan, W.; Cheng, Q.; Xie, Y. *Nano Res.* **2012**, *5*, 521–530; b) Li, J.; Tang, S. B.; Lu, L.; Zeng, H. C. *J. Am. Chem. Soc.* **2007**, *129*, 9401–9409.

18. McCrory, C. C. L.; Jung, S.; Peters, J. C.; Jaramillo, T. F. *J. Am. Chem. Soc.* **2013**, *135*, 16977–16987.

19. Mamaca, N.; Mayousse, E.; Arrii-Clacens, S.; Napporn, T. W.; Servat, K.; Guillet, N.; Kokoh, K. B. *Appl. Catal. B: Environ.* **2012**, *111–112*, 376–380.

20. a) Mao, S.; Wen, Z.; Huang, T.; Hou, Y.; Chen, J. *Energy Environ. Sci.* **2014**, *7*, 609–616; b) Zou, X.; Goswami, A.; Asefa, T. *J. Am. Chem. Soc.* **2013**, *135*, 17242−17245; c) Smith, R. D. L.; Prévot, M. S.; Fagan, R. D.; Trudel, S.; Berlinguette, C. P. *J. Am. Chem. Soc.* **2013**, *135*, 11580−11586.

21. a) Masa, J.; Xia, W.; Sinev, I.; Zhao, A.; Sun, Z.; Grützke, S.; Weide, P.; Muhler, M.; Schuhmann, W. *Angew. Chem.* **2014**, *126*, 8648–8652; *Angew. Chem. Int. Ed.* **2014**, *53*, 8508–8512; b) Han, X. P.; Cheng, F. Y.; Zhang, T. R.; Yang, J. G.; Hu, Y. X.; Chen, J. *Adv. Mater.* **2014**, *26*, 2047–2051.

22. Lu, Z.; Wang, H.; Kong, D.; Yan, K.; Hsu, P. C.; Zheng, G.; Yao, H.; Liang, Z.; Sun, X.; Cui, Y. *Nat. Commun.* **2014**, *5*, 4345.

23. a) Kong, D.; Wang, H.; Lu, Z.; Cui, Y. *J. Am. Chem. Soc.* **2014**, *136*, 4897−4900; b) Faber, M. S.; Dziedzic, R.; Lukowski, M. A.; Kaiser, N. S.; Ding, Q.; Jin, S. *J. Am. Chem. Soc.* **2014**, *136,* 10053–10061.

Table of Contents (TOC)